

# Probing Planck's Law for an Object Thinner than the Thermal Wavelength

C. Wuttke and A. Rauschenbeutel\*

*Vienna Center for Quantum Science and Technology,  
TU Wien – Atominstitut, Stadionallee 2, 1020 Wien, Austria.*

(Dated: June 13, 2022)

We investigate the thermalization via heat radiation of a silica fiber with a diameter smaller than the thermal wavelength. The temperature change of the subwavelength-diameter fiber is determined through a measurement of its optical path length in conjunction with an ab initio thermodynamic model of the fiber structure. The results differ significantly from the predictions of Planck's law based on the spectral emissivity of silica. Excellent agreement is obtained with a theoretical model that considers heat radiation as a volumetric effect and that takes the emitter shape and size relative to the emission wavelength into account. These results are of fundamental interest, may lead to technical applications, and can contribute to improved models of the earth's climate system.

Thermalization via heat radiation is an omnipresent process which, e.g., determines the temperature of stars and planets or the functioning of incandescent lamps. For a perfectly black body, the spectral emissive power of thermal radiation was first explained by Planck [1] who used quantized energies for the radiation field, thereby breaking the grounds for quantum theory. However, a real object does not radiate like a perfectly black body but emits a modified spectrum which can be related to Planck's law by introducing a correction factor, the so-called spectral emissivity [2]. Usually, this spectral emissivity is treated as a surface property that depends on the specific material and the surface roughness. Yet, if the material is not opaque, thermal radiation from within the bulk material can escape into free space provided that its point of emission is closer to the surface than its absorption length in the material. As soon as the latter gets larger than the size of the radiating body, one therefore has to consider thermal radiation as a volumetric effect [3, 4].

Recent experiments have shown that size and geometrical structure of an object may play an important role for the spectrum, coherence, and angular distribution of its thermal radiation [5–9]. Moreover, it has been shown that the radiative heat transfer rate can be strongly enhanced by near-field effects [10]. Here, we optically measure the thermalization of a silica nanofiber with a diameter of 500 nm, smaller than all absorption lengths of the thermal radiation spectrum. The fiber resides in an ultra high vacuum chamber and heat transport is dominated by far-field radiation. Our data shows, to the best of our knowledge for the first time, that the total far-field radiated power of a subwavelength structure deviates from Planck's law and agrees quantitatively with the predictions given by so-called fluctuational electrodynamics (FED) [11].

The silica nanofibers used for our experiment are realized as the waist of a tapered optical fiber (TOF) which is produced from a standard optical fiber in a heat-and-pull process [12, 13]. A temperature change of the nanofiber waist induces a change of its optical path length which is primarily due to the thermo-optic effect of silica. In order to measure this optical path length change, the TOF is enclosed in a fiber-based Fabry-Pérot-type optical resonator which uses two fiber Bragg-gratings (FBGs) as cavity mirrors, see inset of Fig. 1 [14]. In this configuration, the optical path length change is translated into a frequency shift of the Fabry-Pérot resonances which we read out via the transmission of a probe laser field, see Fig. 1. The nanofiber waist is heated by sending a second laser field through the TOF. Its wavelength lies in the transmission band of the FBGs and its power is adjustable by means of an acousto-optic modulator (AOM). A small fraction of this optical power is absorbed along the nanofiber, thereby

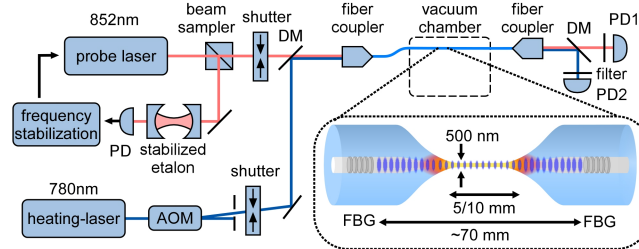


FIG. 1. Schematics of the experimental setup for measuring the thermally induced optical path length change of the optical nanofiber. The inset shows the TOF-resonator with the nanofiber waist.

\* Arno.Rauschenbeutel@ati.ac.at.

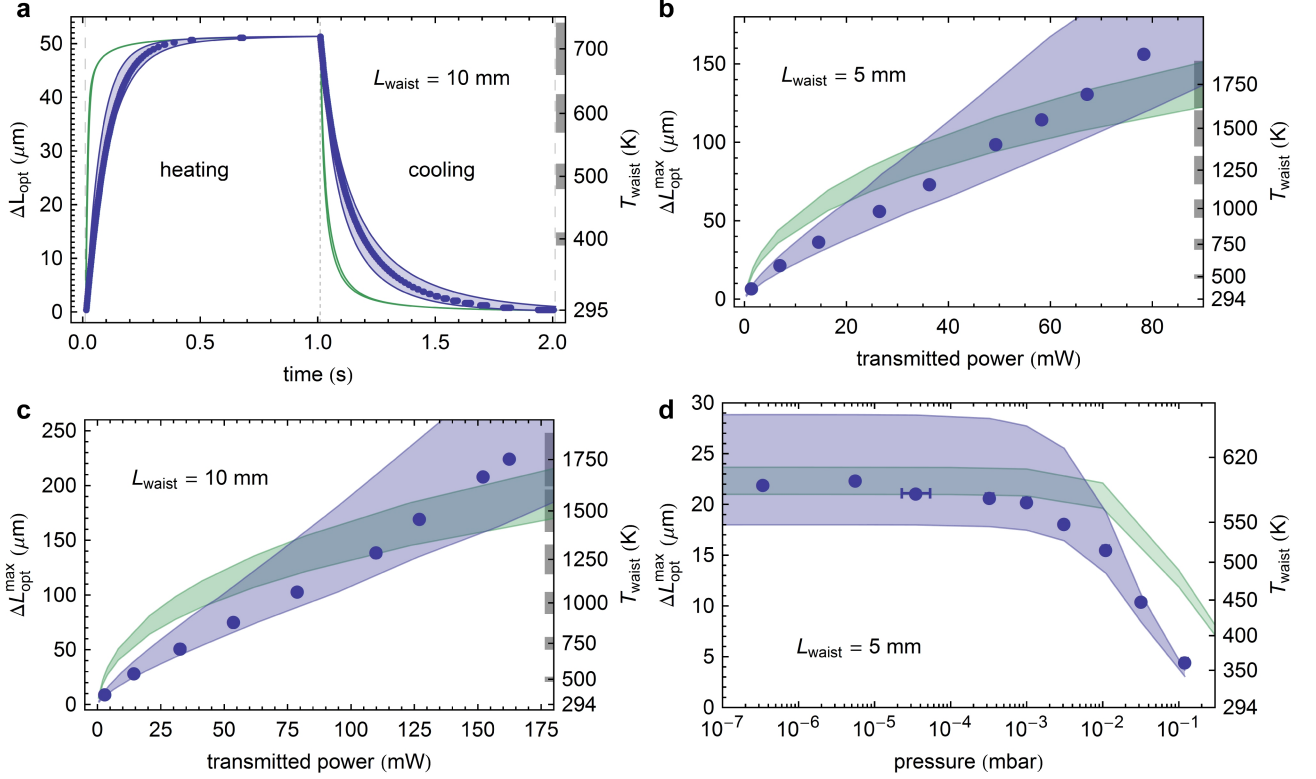


FIG. 2. Thermally induced optical path length change of the silica nanofiber. Circles: Experimental data; blue bands: FED predictions; green bands: predictions using Planck's law. (a) Example of thermalization dynamics. (b-d) Maximum optical path length change as a function of the heating laser power transmitted through the TOF and of the background gas pressure, respectively.

heating the latter. After exiting the TOF, the transmitted probe and heating laser fields are separated by a dichroic mirror (DM) and spectral filters such that their respective powers can be measured independently using photodiodes (PD1 & PD2). By abruptly switching the heating laser beam with a mechanical shutter, the heat source can be turned on and off, allowing us to measure the heating and cooling dynamics of the nanofiber.

For this purpose, we record a time trace of the probe transmission which consists of a sequence of Fabry-Pérot transmission peaks. From one peak to the next, the single-pass intra-cavity optical path length has changed by half the vacuum wavelength of the probe laser,  $\Delta L_{\text{opt}} = \lambda_0/2 = 426$  nm. Prior to each cycle of heating and successive cooling, we establish a reproducible thermal situation by an initializing pulse sequence of the heating laser: First the heating laser power is set to a high value (80–160 mW) and is sent through the TOF for 30 s. This heating time is significantly longer than the thermalization time constant of the unprocessed fiber parts of  $\sim 8$  s, determined in an independent measurement by tracking the central wavelength shift of the FBG stop-band. Then, the heating laser is switched off for 2 s. This cooling time is ten times longer than the thermalization time constant of the nanofiber, see below. This ensures that the nanofiber is thermalized at ambient temperature while the unprocessed fiber exhibits a constant initial condition.

A typical time trace of  $\Delta L_{\text{opt}}$  is shown in Fig. 2a for a TOF-resonator with a waist diameter of  $(500 \pm 50)$  nm, a nominal homogeneous waist length of  $L_{\text{waist}} = 10$  mm, and a finesse of  $85 \pm 1$  (TOF-resonator #1; detailed radius profile in the supplementary informations). For this measurement, the heating laser is switched on between  $t = 0$  s and  $t = 1$  s, the transmitted power is  $P_{\text{heat}} = 32.7(1)$  mW, and the background gas pressure is  $p = 10^{-6}$  mbar. For both the heating and for the cooling process,  $\Delta L_{\text{opt}}$  varies rapidly during the first 500 ms. Following this initial fast dynamics, the variation of  $\Delta L_{\text{opt}}$  takes place on a much longer timescale on the order of several seconds. Because of the discrete nature of the measurement method which relies on counting transmission peaks, one additional data point was added at the end of the heating (cooling) period. Its value is chosen  $\lambda_0/4$  higher (lower) than the last measured data point and its error bar is given by  $\pm \lambda_0/4$ , thereby accounting for the fact that  $\Delta L_{\text{opt}}$  changed by less than  $\lambda_0/2$ .

In order to gain a quantitative understanding of the observed dynamics of  $\Delta L_{\text{opt}}$ , we develop an ab initio thermo-

dynamical model of the TOF including heat transport via thermal radiation, heat conduction along the TOF, and heat diffusion through the surrounding background gas (see supplementary informations). The parameters that enter into the model are the specific heat, the heat conductivity, and the density of silica as well as the molecular mass and the number of degrees of freedom of molecular nitrogen in order to account for the background gas. Furthermore, the model uses the radius profile and the total radiated power per unit length of the TOF. The latter can either be computed according to Planck's law including the spectral emissivity of silica or using FED [15, 16]. It has been shown that the transmission loss of TOFs is primarily governed by surface pollution [17]. In our model, we therefore assume that the heating of the TOF is caused by surface absorption, meaning that the heating power per unit length at any position along the TOF is proportional to the radius-dependent surface intensity of the TOF-guided mode [18], integrated over the circumference. Furthermore, we neglect temperature gradients in the background gas. In our system, this assumption is valid for pressures  $p < 10^{-3}$  mbar. For higher pressures, our model may overestimate the effect of heat diffusion. In the low pressure regime, the largest uncertainties that enter into the model are the radius profile, which is known with a relative error of  $\pm 10\%$  [19, 20], and the wavelength-dependent complex refractive index of fused silica,  $\hat{n}$ . The latter is the sole material property that is used in the FED calculation of the radiated power as well as in the calculation of the spectral emissivity. It was extracted from various literature sources for wavelengths ranging from  $\sim 300$  nm to  $\sim 50$   $\mu\text{m}$  (see supplementary informations).

We numerically solve the two resulting differential equations (Planck and FED) for the same heating and cooling cycle as in the experiment and determine the time-dependent temperature profile along the TOF as a function of the total absorbed optical power,  $P_{\text{abs}}$ , and the background gas pressure. Four different parameter sets are used for these calculations, combining the minimum or maximum TOF radius profile with the values of  $\hat{n}$  that yield the minimum or maximum radiated power per unit length, respectively. From these temperature profiles, we then compute  $\Delta L_{\text{opt}}$  via the temperature-dependent effective refractive index which is integrated along the TOF-resonator (see supplementary informations). The theory bands in Fig. 2a are delimited by the two extremal time traces of  $\Delta L_{\text{opt}}$  that reproduce the maximum observed optical path length change  $\Delta L_{\text{opt}}^{\text{max}}$  (solid lines). We find excellent agreement between the time dependence of  $\Delta L_{\text{opt}}$  predicted by FED and the experimental data while the prediction for Planck's law significantly deviates from the latter.

Figure 2b and c show  $\Delta L_{\text{opt}}^{\text{max}}$  as a function of the heating laser power transmitted through the TOF,  $P_{\text{heat}}$ , for TOF-resonators #1 and #2. The latter corresponds to a TOF with a waist diameter of  $(500 \pm 50)$  nm,  $L_{\text{waist}} = 5$  mm, and a finesse of  $18 \pm 1$ . In both cases,  $\Delta L_{\text{opt}}^{\text{max}}$  increases roughly linearly with  $P_{\text{heat}}$  within the observed power range. In order to analyze the measured data, the ratio  $\eta$  between  $P_{\text{heat}}$  and  $P_{\text{abs}}$  has to be determined. This is done by inserting  $P_{\text{abs}} = \eta P_{\text{heat}}$  into both theories and fitting their predictions independently to the data using the four parameter sets concerning the radius and the complex refractive index. We compute the mean of the minimum and maximum resulting  $\eta$ -value,  $\bar{\eta} = (\eta_{\text{max}} + \eta_{\text{min}})/2$ , for both theories and plot the extremal theory prediction (solid lines delimiting the colored bands) using the corresponding two parameter sets and  $P_{\text{abs}} = \bar{\eta} P_{\text{heat}}$ . For both resonators, the FED prediction is in excellent agreement with the experimental data while the prediction for Planck's law exhibits a significant qualitative deviation.

From the temperature profiles along the TOF which lead to the two extremal predictions of  $\Delta L_{\text{opt}}^{\text{max}}$ , we determine two corresponding extremal predictions for the temperature at the center of the waist,  $T_{\text{waist}}^{\text{max}}$  and  $T_{\text{waist}}^{\text{min}}$ , respectively. The resulting non-linear temperature scale,  $\bar{T}_{\text{waist}} = (T_{\text{waist}}^{\text{max}} + T_{\text{waist}}^{\text{min}})/2$ , where and  $\Delta \bar{T}_{\text{waist}} = (T_{\text{waist}}^{\text{max}} - T_{\text{waist}}^{\text{min}})/2$ , is shown on the right axes of all panels of Fig. 2, with the ticks and the gray bars indicating  $\bar{T}_{\text{waist}}$  and  $\Delta \bar{T}_{\text{waist}}$ , respectively. It covers a temperature range from room temperature to almost 2000 K. While this upper temperature limit exceeds the glass transition temperature of silica of about 1450 K [21], the corresponding viscosity of  $10^6$  Pa·s is still very high and ensures the mechanical stability of the TOF. We note that the temperature scale in Fig. 2a refers to the cooling process. The corresponding scale for the heating process differs from the latter and is not shown for clarity.

Figure 2d shows  $\Delta L_{\text{opt}}^{\text{max}}$  as a function of the background gas pressure for TOF-resonator #2 and  $P_{\text{heat}} = 6.7(2)$  mW. Both the measured values and the theory prediction yield constant results for pressures lower than  $10^{-4}$  mbar, confirming our assumption that heat diffusion through the background gas is negligible for all other measurements presented here, which were performed at pressures below  $10^{-6}$  mbar.

We now analyze the thermalization dynamics for varying heating powers and thus for varying  $\Delta L_{\text{opt}}^{\text{max}}$ . For this purpose, we determine the 10 % – 50 % and 75 % – 90 % rise times (heating) and the 90 % – 50 % and 25 % – 10 % fall times (cooling) of the time traces of  $\Delta L_{\text{opt}}$  in order to quantify the initial and the final dynamical behavior. We find time constants on the order of 100 ms which are plotted in Fig. 3 as a function of  $\Delta L_{\text{opt}}^{\text{max}}$ . The same quantities are derived from the theory predictions for Planck's law and FED, respectively, and plotted as bands in the same graphs. The agreement between the experimental data and the FED predictions is excellent, whereas Planck's law predicts up to one order of magnitude shorter time constants. All theory predictions in this figure are ab initio results without any adjustable parameters.

Summarizing, we present conclusive experimental evidence for the failure of Planck's law in predicting the total

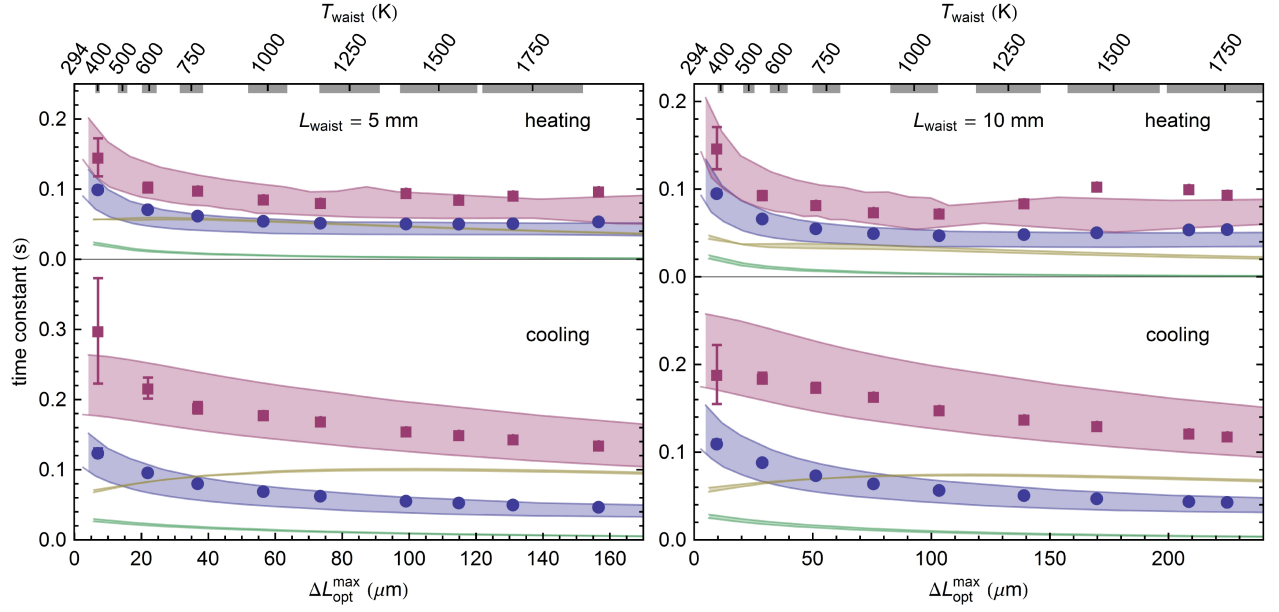


FIG. 3. Thermalization time constants of the silica nanofiber as a function of the maximum optical path length change for the two TOF resonators. Blue circles: measured initial time constants; red squares: final time constants; blue (red) bands: FED predictions for initial (final) time constants; green (yellow) bands: predictions for initial (final) time constants using Planck's law.

thermally radiated power of a silica fiber with a sub-micron diameter. Moreover, we quantitatively confirm that its heat radiation is a volumetric effect and that fluctuational electrodynamics yields an accurate description of this phenomenon. These results have important implications for technical applications, such as heat management in nano-devices or the realization of energy-efficient incandescent lamps. Moreover, they might also lead to a better understanding of the impact of particulate matter, such as mineral dust aerosols from soil erosion and soot from combustion sources, on the climate system via absorption and emission of solar and thermal radiation [22, 23].

## SUPPLEMENTARY INFORMATION

### Optical path length change

The optical path length change has its origin in three basic effects: The thermo-optic and the strain-optic effect of silica, i.e., the temperature- and strain-dependence of its refractive index,  $n$ , as well as the radial thermal expansion of the fiber. All effects lead to a change of the so-called  $V$ -parameter of the vacuum-clad fiber waist [18],  $V = 2\pi a\sqrt{n^2 - 1}/\lambda_0$ , either via a change of  $n$  or via a change of the fiber radius  $a$ . This results in a change of the effective refractive index of the fundamental  $\text{HE}_{11}$  fiber mode in which the light is guided through the TOF,  $n_{\text{eff}} = \beta(V)/k_0$ , where  $\beta(V)$  is the  $V$ -dependent propagation constant of the  $\text{HE}_{11}$  mode [18] and  $k_0 = 2\pi/\lambda_0$ .

The tensile stress of the fiber varies with temperature because of the axial thermal expansion of the fiber: Following the heat-and-pull process, the TOF is pre-strained before fixing it to its mechanical mount, leading to an elongation of the nanofiber waist by  $\Delta L_{\text{strain}}/L_0 = 5 \cdot 10^{-2}$  of its original physical length  $L_0$ . This elongation is much larger than the axial thermal expansion of the nanofiber which, assuming an unstrained nanofiber and a thermal expansion coefficient of silica of  $\alpha_{\text{te}} = (\Delta L/L)/\Delta T = (4 - 7) \cdot 10^{-7} \text{ /K}$  [24], would be of the order of  $\Delta L_{\text{therm}}/L_0 \approx 10^{-3}$  for the maximum measured temperature of 2000 K. As a consequence, the axial thermal expansion of the nanofiber does not modify the length of the pre-strained nanofiber but rather lowers its tensile stress. This leads to a change of  $n$  via the strain-optic effect and to an increase of  $a$  due to the reduced transversal contraction of the nanofiber.

The thermally-induced change of the effective refractive index for a given fiber radius is thus given by:

$$\frac{dn_{\text{eff}}(a, T)}{dT} = \frac{\partial n_{\text{eff}}(a)}{\partial n} \left( \frac{\partial n(T)}{\partial T} - n \alpha_{\text{te}}(T) \alpha_{\text{so}} \right) + \frac{\partial n_{\text{eff}}(a)}{\partial a} (1 + \mu_P) \alpha_{\text{te}}(T) a, \quad (1)$$

where  $\partial n(T)/\partial T$  is the thermo-optic coefficient of silica,  $\alpha_{\text{so}} = (\Delta n/n)/(\Delta L_{\text{strain}}/L_0) = -0.206$  is the stress-optic coefficient of silica [25], and  $\mu_P = -0.168$  is Poisson's ratio for silica [25].

In the literature, the thermo-optic coefficient of silica is well characterized for room temperature. However, few studies have been carried out for temperatures exceeding  $\sim 800 \text{ K}$ . To our knowledge, the widest temperature range (300 K – 1570 K) has been characterized using the thermally induced wavelength shift of a FBG-mirror stop-band  $\Delta \lambda_B$  [26]. From the latter, the thermo-optic coefficient has been extracted for a wavelength of  $\sim 1570 \text{ nm}$  by using

$$\frac{1}{\lambda_B} \frac{d\lambda_B}{dT} = \left[ (1 - \alpha_{\text{so}}) \alpha_{\text{te}}(T) + \frac{1}{n} \frac{\partial n(T)}{\partial T} \right] \quad (2)$$

where  $\lambda_B$  is the central wavelength of the FBG stop-band [27]. Based on this data, we applied an established model that predicts the dispersion of the thermo-optic coefficient [28] to compute its value at the probe wavelength of  $\lambda_0 = 852 \text{ nm}$  used in our experiment. By fitting the temperature-dependent refractive index change with a 2nd-order polynomial function (coefficient of determination:  $R^2 = 1 - 6 \cdot 10^{-6}$ ) and by differentiating the latter with respect to the temperature, we obtain the temperature dependent thermo-optic coefficient:

$$\frac{n(T)}{\partial T} = 9.627(9) \cdot 10^{-6} + 7.74(1) \cdot 10^{-9} (T - 299 \text{ K}) \quad (3)$$

We compared the prediction of our fit with values extracted from several literature sources that use various methods [27–30] and find a relative error of the predicted refractive change index change with respect to the literature values of  $\Delta(\partial n/\partial T)/(\partial n/\partial T) < 10 \%$ . We note that the data from all cited works also qualitatively agrees with the temperature dependence predicted by Eq. 3. We also note that, to our knowledge, the thermal expansion coefficient is known up to 1000 K [24]. For higher temperatures we therefore employ a linear extrapolation of the two highest temperature values measured in [24].

The resulting thermal change in the effective refractive index is plotted as function of temperature in Fig. 4. In all the above considerations, the effect of the fiber core has been neglected. This is justified because the core constitutes a negligible fraction ( $< 0.5 \%$ ) of the fiber material which contributes to the guiding of the light in the nanofiber section and, in addition, has similar optical properties as the cladding material.

### The TOF radius profile

The tapered optical fibers used in this experiment are produced from standard single-mode optical fibers with a cladding diameter of  $125 \mu\text{m}$ . For this purpose, we employ a custom-built computer-controlled fiber pulling rig which allows us to fabricate TOFs with a predetermined radius profile. We chose a TOF radius profile which includes a

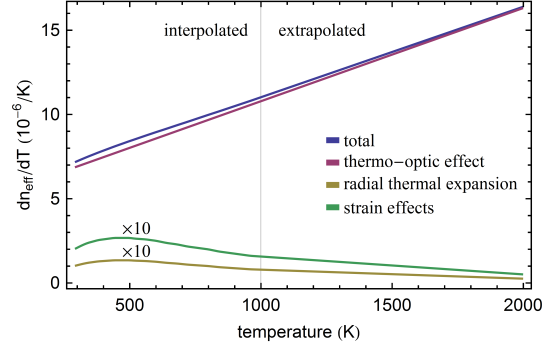


FIG. 4. Temperature dependence of the effective thermo-optic coefficient and its contributions for a fiber diameter of 500 nm.

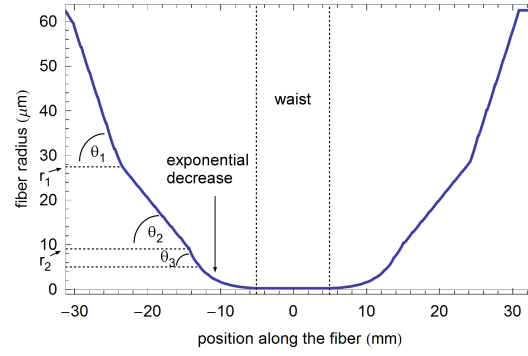


FIG. 5. Simulated radius profile of the tapered section of TOF-resonator #1.

nanofiber waist with a constant subwavelength diameter that is enclosed symmetrically by two fiber tapers as shown in Fig. 5. In a standard optical fiber, the light is guided by the core-cladding interface whereas in the nanofiber section the core has a negligible effect and the light is guided the cladding-vacuum interface. In these subwavelength optical nanofibers, a significant fraction of the optical power propagates outside of the fiber in the form of an evanescent wave that extends several hundred nanometers into the vacuum. A standard fiber exhibits a small refractive index difference between the core and the cladding and the fundamental fiber mode can be approximated by the weakly guided  $LP_{01}$ -mode. To reach a high transmission through the TOF, this mode has to be adiabatically transformed by the taper transition to match the fundamental  $HE_{11}$ -mode of the strongly guiding nanofiber [18]. This is achieved by a taper profile that is composed of three linear sections followed by an exponential decrease adjacent to the waist (see Fig. 5 for TOF-resonator #1). In the first and third linear section of the taper, the fiber diameter is reduced with comparably large angles,  $\Theta_1$  and  $\Theta_3$ , whereas in the second linear section, the transition from a core- to cladding-guided mode takes place and the angle  $\Theta_2$  has to be chosen small enough to ensure an adiabatic transformation.

The TOFs used in the experiment are produced from Fibercore SM800 single mode optical fibers, using the parameters given in Tab. I, where  $r_1$  and  $r_2$  are the cladding radii at the transitions between the linear taper sections. Previous measurements have shown that the actual TOF radius profile agrees with the simulated radius profile within

sample	$\Theta_1$	$\Theta_1$	$\Theta_1$	$L_{\text{waist}}$
TOF-resonator #1	5 mrad	2 mrad	4 mrad	10 mm
TOF-resonator #2	5 mrad	2 mrad	4 mrad	5 mm

TABLE I. Parameters of the two TOF radius profiles of the two samples used in this experiment.

the measurement accuracy of  $\sim 10\%$  [19, 20].

### Thermodynamical model

We model the system including heat transport via radiation, heat conduction in silica, and heat diffusion through the surrounding gas. The assumption that no temperature gradients appear in the surrounding background gas is valid for mean free path lengths that are much larger than the distance from the fiber to the heat sink, such as, e.g., the fiber mount or the vacuum chamber wall. We estimate the pressure up to which this condition is fulfilled by assuming a typical distance to the heat sink in our system of 10 cm and thereby obtain  $p < 10^{-3}$  mbar. We note, however, that the transition to the regime in which the background gas exhibits a temperature gradient can take place in a pressure range that covers several orders of magnitude. For this reason, we also performed an experimental check of the validity of our assumption, see Fig. 2d in the article. The system can then be described by the following differential equation in units of power [31]:

$$c_p \rho \partial_t T dV = \nabla(\lambda \nabla T) dV - \sqrt{\frac{k_b f^2}{8\pi M_{N_2} T_0}} p (T - T_0) dS - dH_{\text{radiative}} + dP_{\text{heating}} \quad (4)$$

where  $dP_{\text{heating}}$  is a heat source, the remaining quantities are given in Tab. II, and the dependencies on space and time are omitted for clarity. The radiated heat  $dH_{\text{radiative}}$  can be either calculated using Planck's law in combination

symbol	description	value from $T_0$ to the highest temperature covered in Ref.	temperature range covered in Ref.	Ref.
$T_0$	room temperature	$(294 \pm 0.5)$ K	-	-
$\lambda$	heat conductivity	$(1.3 - 2.1)$ W/(K·m)	$(0.1 - 1650)$ K	[32]
$c_p$	specific heat (silica)	$(700 - 1500)$ J/(kg·K)	$(0 - 2000)$ K	[33]
$\rho$	density (silica)	2200 kg/m <sup>3</sup>	-	[32]
$f$	degrees of freedom of N <sub>2</sub>	6	-	-
$M_{N_2}$	molecular mass of N <sub>2</sub>	$4.653 \cdot 10^{-26}$ kg	-	-
$k_b$	Boltzmann's constant	$1.381 \cdot 10^{-23}$ J/K	-	-

TABLE II. Model parameters and their values with references.

with the spectral emissivity of a silica–vacuum interface (see below) or using the predictions from FED calculations [15, 16].

We assume the fiber is heated via surface absorption so that the local heating power per unit length is given by the local surface intensity  $I(a(x))$  of the fiber mode multiplied by the fiber circumference  $\partial_x P_{\text{heat}}(x) = 2\pi a(x) I(a(x))$ . Due to the small diameter of the nanofiber, we assume that it exhibits a constant temperature across its diameter. Moreover, the fiber exchanges a negligible amount of heat with the vacuum chamber which, therefore, stays at room temperature during the experiment. This allows us to reduce the equation to one dimension in space along the fiber axis ( $x$ -axis). After differentiating the resulting equation with respect to  $x$ , we then find the following differential equation in units of power per length :

$$\pi a^2 c_p \rho \partial_t T = \pi a^2 \partial_x (\lambda \partial_x T) - \sqrt{\frac{k_b f^2}{8\pi M_{N_2} T_0}} p (T - T_0) 2\pi a - \partial_x H_{\text{radiative}} + \partial_x P_{\text{heating}} \quad (5)$$

where  $\partial H_{\text{radiative}}$  describes the radiated power per unit length. This equation is solved numerically for a given radius profile using the method of lines implemented in Mathematica with a spatial discretization of 0.1 mm along the fiber axis for a TOF section that extends at least 1 cm beyond either side of the waist:  $L_{\text{sim}} = L_{\text{waist}} + 2$  cm. At these points, the fiber diameter has increased to  $\sim 10$   $\mu\text{m}$  and is thus a factor of 20 larger than the waist diameter. As a consequence, the evanescent field and hence the heating power vanishes and the heat capacity per unit length increases by a factor of 400. The boundary conditions are chosen such that the fiber is thermalized to ambient temperature at the beginning of the simulation  $T(t = 0, x) = T_0$  and no heat flow occurs at the boundary of the simulation cell:  $\partial_x T(t, \pm L_{\text{sim}}/2) = 0$ . By solving Eq. 5, we obtain a temperature profile as a function of time and position along the fiber,  $T(t, x)$ . We then use the latter to compute the optical path-length for discrete time-steps via the thermally induced effective refractive index change (see supplementary informations) and compare the results from this simulation to the data.

As discussed above, the largest uncertainties that enter into the simulation are the fiber radius and the complex refractive index of fused silica. Therefore, we solve the Eq. 5 for the maximum and minimum values of the complex refractive index values for type III and IV fused silica available in literature [34] with the radius profile scaled by 90 % and 110 %.

### Complex refractive index of fused silica

The complex refractive index,  $\hat{n} = n + ik$ , is the sole material property that enters the calculation of the spectral emissive power of thermal radiation. We take the uncertainty of the literature values into account by using all four combinations of the maximum and minimum of each  $n$  (refractive index) and  $k$  (extinction coefficient), respectively, in order to compute the total radiated power. We then use the maximum and minimum value of the latter for our further calculations.

Optical fibers are made of high-quality synthetic fused silica, which is an amorphous glass, with a core with typically a few weight percent of dopants such as, e.g., germanium. Four types of fused silica are commercially available [34]: Type I and Type II are produced from crystal quartz by electric melting and from quartz powder by flame fusion, respectively, whereas Type III and Type IV glasses are synthetic glasses produced from  $\text{SiCl}_4$  in a  $\text{H}_2\text{-O}_2$  flame and in a water-vapor free plasma flame respectively. The synthetically produced glasses feature the lowest impurity content and, thereby, exhibit a higher transmission than the Type I and Type II glasses, in particular in the near-infrared and in the ultraviolet spectral ranges.

Since our TOF fabrication employs a  $\text{H}_2\text{-O}_2$  flame for the tapering process, we consider the glass in the TOF to be a mixture of Type III and Type IV silica. We therefore extract the minimum and maximum values of both  $n$  and  $k$ , respectively, that are available for these two types of glass for our calculations. For wavelength regions in which we did not encounter literature values for these particular types of glass, we also use data for other types of fused silica. The resulting minimum and maximum contributions of the complex refractive index that we employ for our calculations were derived from [34] and are shown in Fig. 6 as function of the optical wavelength.

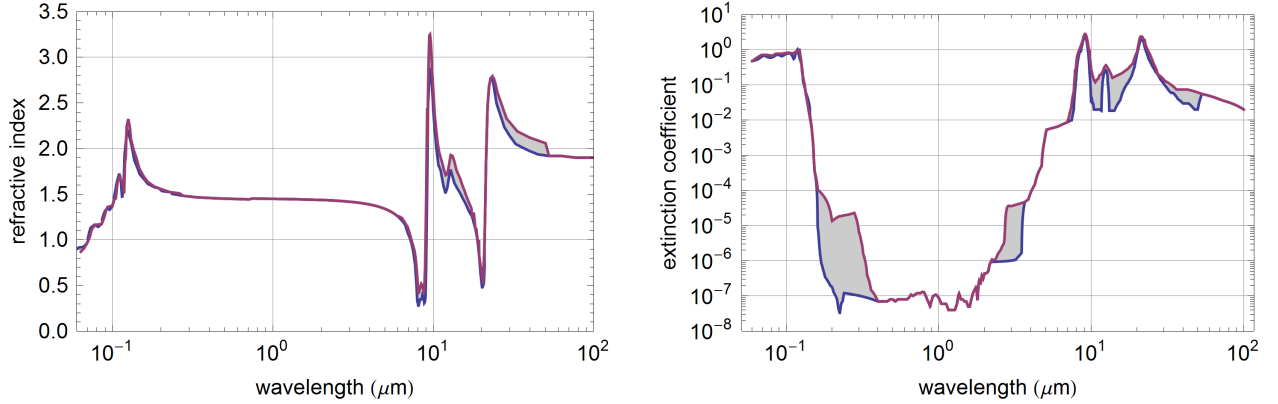


FIG. 6. Refractive index and extinction coefficient of fused silica as function of the wavelength. Red curve: maximum value; blue curve: minimum value.

We note that the values given for the extinction coefficient in the visible spectrum are at the lower limit of the parameter range that is experimentally accessible and therefore can be considered as maximum values. Since no further data is available and heat radiation in the visible spectrum contributes only marginally to the total heat transfer rate, we do not consider smaller values.

### Emissivity of a silica–vacuum interface

We now sketch the steps that are necessary for computing the emissivity of a polished silica–vacuum interface. A comprehensive treatment of thermal radiation of surfaces can be found in the literature [2, 35]. The total thermally radiated power of an object can be calculated by using the Stefan-Boltzmann equation  $H(T) = \epsilon(T) \sigma_B T^4 A$ , where  $A$  is the surface area of the object,  $\sigma_B$  is the Stefan-Boltzmann constant, and  $\epsilon(T)$  is the total hemispherical emissivity. The latter can be derived using Kirchhoff’s law, which states that the emissivity of an interface is equal to its absorptivity. For a semi-infinite silica–vacuum interface, all light that enter the silica will be absorbed. For this reason, the directional spectral emissivity is given by  $\epsilon(\nu, \Omega) = 1 - R(\nu, \Omega)$ , where  $\nu$  is the optical frequency,  $\Omega = \{\theta, \phi\}$  stands for the polar and the azimuthal angle, and  $R(\nu, \Omega)$  is the directional spectral reflectivity. By using Planck’s law for the spectral emissive power,

$$W(\nu, T) = \frac{2\nu^2}{c^2} \frac{h\nu}{\exp(h\nu/k_B T) - 1} \quad (6)$$



the total hemispherical emissivity can then be computed:

$$\epsilon(T) = \frac{\int d\Omega \int d\nu W(\nu, T) \epsilon(\nu, \Omega) \cos(\theta)}{\sigma_B T^4} \quad (7)$$

where  $d\Omega = \sin(\theta)d\theta d\phi$ . The directional spectral reflectivity can be derived from Frensel's formula for absorbing media by averaging over both polarizations [36]:

$$\rho_{\text{refl.}} = \frac{1}{2} \left( \left| \frac{\hat{n}_1(\nu) \cos(\theta_1) - \hat{n}_2(\nu) \cos(\theta_2)}{\hat{n}_1(\nu) \cos(\theta_1) + \hat{n}_2(\nu) \cos(\theta_2)} \right|^2 + \left| \frac{\hat{n}_2(\nu) \cos(\theta_1) - \hat{n}_1(\nu) \cos(\theta_2)}{\hat{n}_1(\nu) \cos(\theta_1) + \hat{n}_2(\nu) \cos(\theta_2)} \right|^2 \right), \quad (8)$$

where  $\hat{n}_1$  and  $\theta_1$  are the complex refractive index and the angle of incidence in vacuum, respectively,  $\hat{n}_2$  and  $\theta_2$  are the complex refractive index and the refracted angle in silica, respectively. The angle  $\theta_2$  is obtained from the generalized form of Snell's law for absorbing media [37]:

$$\gamma = \text{Re}(\hat{n}_1)^2 - \text{Im}(\hat{n}_1)^2 + \sin(\theta_1)^2, \quad \kappa = (\text{Re}(\hat{n}_1)^2 - \text{Im}(\hat{n}_1)^2) \sin(\theta_1)^2 - \text{Re}(\hat{n}_1)^2 \text{Im}(\hat{n}_1)^2 \quad (9)$$

$$\theta_2 = \arcsin \left( \frac{\sin(\theta_1)}{n'} \right), \quad \text{with} \quad n' = \sqrt{\frac{\gamma}{2} \left( 1 \pm \sqrt{1 - 4\kappa/\gamma^2} \right)} \quad (10)$$

The total hemispherical emissivity is plotted in Fig. 7 as a function of temperature for all combinations of the maximum and minimum values of the real and imaginary part of the refractive index. As explained in the main text of the

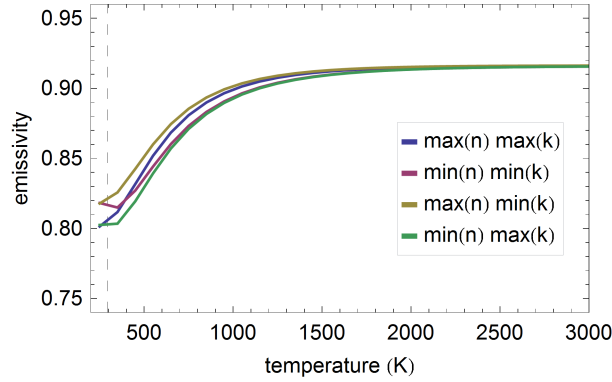


FIG. 7. Emissivity of a polished silica-vacuum interface as function of temperature.

manuscript, only the minimum and maximum emissivity traces (green and yellow lines, respectively) are used for further calculations.

- 
- [1] M. Planck, "Ueber das Gesetz der Energieverteilung im Normalspectrum," *Ann. Phys.* **309**, 533 (1901).
  - [2] R. Siegel and J. R. Howell, *Thermal radiation heat transfer* (McGraw-Hill, 1972).
  - [3] K. Joulain, J.-P. Mulet, F. Marquier, R. Carminati, and J.-J. Greffet, "Surface electromagnetic waves thermally excited: Radiative heat transfer, coherence properties and Casimir forces revisited in the near field," *Surf. Sci. Rep.* **57**, 59 (2005).
  - [4] V. P. Carey, G. Chen, C. Grigoropoulos, M. Kaviani, and A. Majumdar, "A review of heat transfer physics," *Nanoscale Microsc. Therm.* **12**, 1 (2008).
  - [5] J.-J. Greffet, R. Carminati, K. Joulain, J.-P. Mulet, S. Mainguy, and Y. Chen, "Coherent emission of light by thermal sources," *Nature* **416**, 61 (2002).
  - [6] Y. Fan, S. B. Singer, R. Bergstrom, and B. C. Regan, "Probing Planck's law with incandescent light emission from a single carbon nanotube," *Phys. Rev. Lett.* **102**, 187402 (2009).
  - [7] J. A. Schuller, T. Taubner, and M. L. Brongersma, "Optical antenna thermal emitters," *Nat. Photonics* **3**, 658 (2009).
  - [8] S. Shen, A. Narayanaswamy, and G. Chen, "Surface phonon polaritons mediated energy transfer between nanoscale gaps," *Nano Lett.* **9**, 2909 (2009).
  - [9] Y. Liu, C. Meng, A. P. Zhang, Y. Xiao, H. Yu, and L. Tong, "Compact microfiber Bragg gratings with high-index contrast," *Opt. Lett.* **36**, 3115 (2011).

- [10] E. Rousseau, A. Siria, G. Jourdan, S. Volz, F. Comin, J. Chevrier, and J.-J. Greffet, “Radiative heat transfer at the nanoscale,” *Nat. Photon.* **3**, 514 (2009).
- [11] S. M. Rytov, Y. A. Kravtsov, and V. I. Tatarskii, *Principles of statistical radiophysics*, vol. 3 (Springer, Berlin, 1978).
- [12] T. A. Birks and Y. W. Li, “The shape of fiber tapers,” *J. Lightwave Technol.* **10**, 432 (1992).
- [13] F. Warken, A. Rauschenbeutel, and T. Bartholomäus, “Fiber pulling profits from precise positioning,” *Photon. Spectra* **42**, 73 (2008).
- [14] C. Wuttke, M. Becker, S. Brückner, M. Rothhardt, and A. Rauschenbeutel, “Nanofiber Fabry-Pérot microresonator for non-linear optics and cavity quantum electrodynamics,” *Opt. Lett.* **37**, 1949 (2012).
- [15] M. Krüger, T. Emig, and M. Kardar, “Nonequilibrium electromagnetic fluctuations: Heat transfer and interactions,” *Phys. Rev. Lett.* **106**, 210404 (2011).
- [16] V. A. Golyk, M. Krüger, and M. Kardar, “Heat radiation from long cylindrical objects,” *Phys. Rev. E* **85**, 046603 (2012).
- [17] M. Fujiwara, K. Toubaru, and S. Takeuchi, “Optical transmittance degradation in tapered fibers,” *Opt. Express* **19**, 8596 (2011).
- [18] A. Yariv, *Optical Electronics* (Saunders College Publishing, Philadelphia, 1991).
- [19] U. Wiedemann, K. Karapetyan, C. Dan, D. Pritzkau, W. Alt, S. Irsen, and D. Meschede, “Measurement of submicrometre diameters of tapered optical fibres using harmonic generation,” *Opt. Express* **18**, 7693 (2010).
- [20] A. Stiebeiner, R. Garcia-Fernandez, and A. Rauschenbeutel, “Design and optimization of broadband tapered optical fibers with a nanofiber waist,” *Opt. Express* **18**, 22677 (2010).
- [21] R. H. Doremus, “Viscosity of silica,” *J. Appl. Phys.* **92**, 7619 (2002).
- [22] U.S. Climate Change Science Program, *Vision for the program and highlights of the scientific strategic plan*, (USGCRP Publication, 2003; <http://www.climatechange.gov/Library/stratplan2003/vision/ccsp-vision.pdf>).
- [23] H. Liao and J. Seinfeld, “Radiative forcing by mineral dust aerosols: sensitivity to key variables,” *J. Geophys. Res.* **103**, 31637 (1998).
- [24] National Institute of Standards and Technology, *Certificate for standard reference material 739: Fused-silica thermal expansion*, (NIST certificate, 1991, <https://www-s.nist.gov/srmors/certificates/archive/739.pdf>).
- [25] N. F. Borrelli and R. A. Miller, “Determination of the individual strain-optic coefficients of glass by an ultrasonic technique,” *Appl. Opt.* **7**, 745 (1968).
- [26] C. Liao, D.-N. Wang, Y. Li, T. Sun, and K. T. V. Grattan, “Temporal thermal response of Type II-IR fiber Bragg gratings,” *Appl. Opt.* **48**, 3001 (2009).
- [27] S. Pal, T. Sun, K. T. Grattan, S. A. Wade, S. F. Collins, G. W. Baxter, B. Dussardier, and G. Monnom, “Non-linear temperature dependence of Bragg gratings written in different fibres, optimised for sensor applications over a wide range of temperatures,” *Sensor. Actuator.* **112**, 211 (2004).
- [28] E. Palik, *Handbook of thermo-optic coefficients of optical materials with applications*, vol. 3 (Academic Press, London, 1998).
- [29] J. H. Wray and J. T. Neu, “Refractive index of several glasses as a function of wavelength and temperature,” *J. Opt. Soc. Am.* **59**, 774 (1969).
- [30] C. Tan and J. Arndt, “Temperature dependence of refractive index of glassy SiO<sub>2</sub> in the infrared wavelength range,” *Journal of Physics and Chemistry of Solids* **61**, 1315 (2000).
- [31] W. Demtröder, *Experimentalphysik 1*, vol. 1 (Springer Berlin / Heidelberg, 2003), 3rd ed.
- [32] J. J. Freeman and A. C. Anderson, “Thermal conductivity of amorphous solids,” *Phys. Rev. B* **34**, 5684 (1986).
- [33] J. Horbach, W. Kob, and K. Binder, “Specific heat of amorphous silica within the harmonic approximation,” *J. Phys. Chem. B* **103**, 4104 (1999).
- [34] R. Kitamura, L. Pilon, and M. Jonasz, “Optical constants of silica glass from extreme ultraviolet to far infrared at near room temperature,” *Appl. Opt.* **46**, 8118 (2007).
- [35] J. H. I. Lienhard and J. H. V. Lienhard, *A Heat Transfer Text Book* (Phlogiston Press, 2011), 4th ed.
- [36] J. D. Jackson, *Classical Electrodynamics* (Wiley, New York, 1999), 3rd ed.
- [37] P. E. Ciddor, “Refraction into an absorbing medium,” *American Journal of Physics* **44**, 786 (1976).

## ACKNOWLEDGMENTS

We thank the group of Manfred Rothhardt for the fabrication of the fiber Bragg grating mirrors, Michaela Ponweiser for her help in developing the thermal initialization procedure as well as V. Golyk and M. Krüger for helpful discussions and for providing us with the source code of their FED-model. We gratefully acknowledge financial support by the Volkswagen Foundation (Lichtenberg Professorship), the European Science Foundation (EURYI Award), and NanoSci-E+ (NOIs project).